NANO LETTERS
Letter
Cite This: Nano Lett. 2018, 18, 4034−4039
pubs.acs.org/NanoLett

Constructing Highly Porous Thermoelectric Monoliths with High-Performance and Improved Portability from Solution-Synthesized Shape-Controlled Nanocrystals

Biao Xu,[*,†,‡] Tianli Feng,[§,∥] Zhe Li,[‡] Sokrates T. Pantelides,[§,∥] and Yue Wu[*,‡]

[†]School of Chemical Engineering, Nanjing University of Science and Technology, Nanjing, Jiangsu 210094, China
[‡]Department of Chemical and Biological Engineering, Iowa State University, Ames, Iowa 50011, United States
[§]Department of Physics and Astronomy and Department of Electrical Engineering and Computer Science, Vanderbilt University, Nashville, Tennessee 37235, United States
[∥]Materials Science and Technology Division, Oak Ridge National Laboratory, Oak Ridge, Tennessee 37831, United States

Supporting Information

ABSTRACT: Thermoelectricity offers a viable and reliable solution to convert waste heat into electricity. To enhance the performance and portability of thermoelectric materials, the crystal grain and pore structure should be simultaneously manipulated to achieve high electrical conductivity (σ), low thermal conductivity (κ), high figure of merit (zT), and low relative density. However, they cannot be synchronously realized using nanocrystals with uncontrolled domain size and shape as building blocks. Here, we employ solution-synthesized PbS nanocrystals with large grain size, controllable shape and tunable spatial packing to realize the aforementioned structural tuning. The as-sintered highly porous and well crystalline monolith exhibits high σ, low κ, high zT (1.06 at 838 K) and low relative density (82%). The phonon transport is studied by density functional theory highlighting the crucial role of phonon−pore scattering in reducing κ to enhance zT. Our strategy may benefit thermoelectrics and shed light on other technical fields such as catalysis, gas sensing, photovoltaics, and so forth.

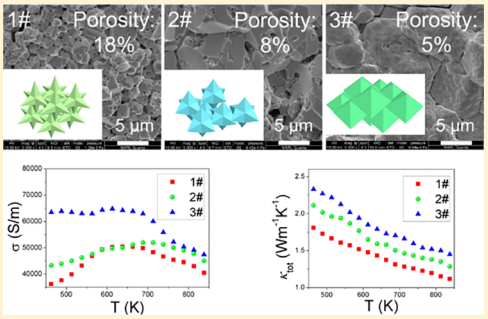

KEYWORDS: *Shape-control, nanocrystal, porous, thermoelectric*

Solution-synthesized, shape-controlled nanoparticles are unique building blocks that have shape-dependent properties with potential applications in diverse technical fields.[1−3] Assembly of these shape-engineered nanocrystals into macroscopic nanostructured solids further endow them with collective[4,5] and synergistic properties.[6−8] Especially, the spatial packing that is influenced by the shape of nanocrystals[9−11] and determines the mesoscale structure can significantly affect various properties of the as-assembled material.[12,13]

Thermoelectrics can convert waste heat into electricity, helping to meet the worldwide energy needs as well as providing power sources in extreme conditions.[14,15] The performance (conversion efficiency) of thermoelectric materials is evaluated by the dimensionless figure of merit, $zT = S^2\sigma T/\kappa$, whose improvement requires increases in the Seebeck coefficient (S)[16,17] and the electrical conductivity (σ)[18] through band engineering, as well as reduction of the thermal conductivity (κ) by modulating the phonon scattering centers at various length scales.[19,20] Aside from performance, the mass density (ρ) is also a critical concern that is relevant to the portability of thermoelectric devices but it is usually ignored. Conventionally, fully dense ingots with high ρ/ρ_0 are used in thermoelectrics to achieve high σ and zT.[17,21] Given the limited categories of thermoelectric materials and their high single-crystal density (ρ_0), a common way to reduce ρ is by creating a porous structure. Existing strategies include using irregularly shaped nanocrystals with poor crystallinity and applying low sintering temperature/axial pressure.[22,23] These approaches usually yield uncontrollable porosity ($\Phi = 1 - \rho/\rho_0$) and small grain size. As a result, although the thermal conductivity can be reduced, the carrier mobility and electrical conductivity are severely impaired, leading to deteriorated zT.

We anticipate that by employing solution-synthesized, shape-controlled nanocrystals with controllable single-unit structure and collective spatial packing, the nanoscale (grain) and mesoscale (pore) structures of as-assembled monoliths can be simultaneously tuned, generating thermoelectric materials with high σ, low κ, high zT and low ρ/ρ_0. However, the thermoelectric evaluation requires large quantities of nano powders (≈ 10 g) to be fabricated into macroscopic monoliths (length >10 mm) for which the large-scale production of shape-controlled nanoparticles is still a challenge.

Received: April 25, 2018
Revised: May 24, 2018
Published: May 28, 2018

DOI: 10.1021/acs.nanolett.8b01691
Nano Lett. 2018, 18, 4034−4039

In this study, we demonstrate a new strategy to simultaneously tune the performance and relative density of thermoelectric materials, using large-scale, solution-synthesized, shape-controlled face-centered-cubic (fcc) PbS nanocrystals as building blocks. The outer contour and packing styles can strongly influence the filling fraction of the assembled macroscopic pellet, lowering the relative density (ρ/ρ_0) and the thermal conductivity (κ). Meanwhile, the crystallinity is maintained high due to the single-crystal nature of building blocks and high sintering temperature, leading to high electrical performance (σ) and zT. We foresee that this paradigm can be generally applied to many other thermoelectric compounds and even materials used in other technical fields such as catalysis, gas sensing, and optoelectronics in which porous structures play a major role.

We first attempted to synthesize PbS nanocrystals with different shapes, especially in terms of convexity (higher convexity indicates longer and sharper protruding arms), which could be deliberately tuned by the reaction time of solution synthesis.[24] To initiate the reaction, the precursors (lead acetate trihydrate and thioacetamide) are dissolved into water and heated. The thioacetamide decomposes into S^{2-} and precipitates with Pb^{2+} to yield PbS. Meanwhile, the surfactant, cetyltrimethylammonium bromide (CTAB) adsorbs onto the surface of the small nuclei of PbS and influences the crystal growth.

At the early stage of reaction (5 h), hexapods (1#) are obtained (Figure 1a). Detailed analysis through the fast Fourier transform (FFT) of high-resolution transmission electron microscopy (HRTEM) image reveals that the tip axis is [0 0 1] (Figure 1b). These tips can be viewed as grown from six (0 0 1) facets of a seed nanocube (Figure S4a). As the reaction proceeds, less-protruding hexapods (2#) are formed (Figure 1c). Finally, octahedra (3#) enclosed by {1 1 1} facets (Figure 1e) are obtained at 48 h and they can be observed along different orientations in the HRTEM (Figures 1f and S1). According to the FFT patterns (Figures 1b,d,f) and TEM images (Figures 1a,c,e) of these nanocrystals, they are single crystalline with domain sizes of 790, 450, and 410 nm, respectively. These nanocrystals form the basis of large grain sizes in the as-sintered pellets. They were further characterized by several techniques. X-ray diffraction (XRD, Figure S2) confirmed that all of them are phase-pure PbS (Galena, rock-salt structure). Energy dispersive spectrum (EDS) detected that apart from Pb (52.0 atom %) and S (46.2 atom %), a tiny amount (1.8 atom %) of Br was distributed throughout the sample. The presence of Br may stem from the incorporation of Br of the surfactant (CTAB) into the nanocrystals during the solution synthesis.

Besides the hexapods, less-protruding hexapods, and perfect octahedra, other series of nanocrystals of which the arms along the [1 0 0] axis are shortened into rectangular-shaped ones can be synthesized under a sulfur-rich condition. In the early stage of reaction (5 h), hexapods are obtained (Figure S3a). As the reaction proceeds (24 h), convex cubes with protruding {1 0 0} facets are formed (Figures S3b,d–f). Finally (48 h), vertex-truncated cubes are formed (Figure S3c).

Having successfully synthesized nanocrystals with different shapes in large quantities (≈ 6.4–10.6 g, see Experimental Section of the Supporting Information), we can consolidate them into macroscopic monoliths using spark plasma sintering (SPS). SPS is a fast (~10 min) and efficient sintering technique during which grain growth can be mitigated.[22] After SPS,

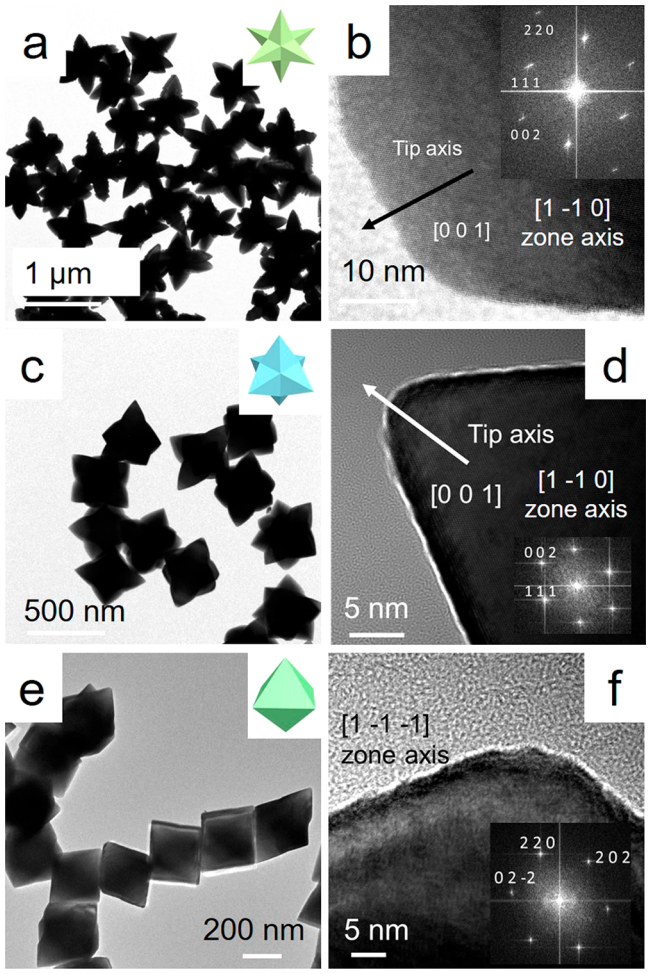

Figure 1. (a,c,e) Low-magnification TEM images of 1# (hexapod), 2# (less-protruding hexapod), and 3# (octahedron) nanocrystals, respectively, the insets show corresponding geometrical models. (b,d,f): HRTEM images and FFT patterns of 1#, 2#, and 3# nanocrystals, respectively. The scale bars in (a–f) are 1 μm, 10 nm, 500 nm, 5 nm, 200 nm, and 5 nm, respectively.

obvious differences in the relative density (1#, 82.2%; 2#, 92.0%; and 3#, 95.1%) were found among various samples (Figures 2d–f) starting from nanocrystals with decreasing convexities (lower convexity indicates shorter and less-protruding arms, from 1# to 3# in Figures 2a–c). The trend in the porosity after sintering can be conjectured in the context of the spatial stacking of the building blocks. For the hexapod retrieved at the earliest stage of solution synthesis, we propose one possible packing style in which the hexapods are stacked in the space in a simple cubic symmetry and the arms are attached antiparallelly to the arms of the neighboring hexapod (Figures 2a and S4). This is like the "pod–pod" parallel configuration of octapods[25] as depicted in the reference. The calculated filling fraction is 24.2%. Although this may not be the densest packing, it demonstrates that the hexapods tend to pack in a low relative density. By decreasing the convexity (with less-protruding arms), this filling fraction can be increased to 34.1% (Figure S5) and even 50.6%. Moreover, the relative density of the octahedron-sintered sample (3#) can be as high as 95.1% after the sintering process, which agrees with the theoretically calculated 94.7% of the densest packing.[10] From these results, the correlation between convexity and packing density can be

DOI: 10.1021/acs.nanolett.8b01691
Nano Lett. 2018, 18, 4034–4039

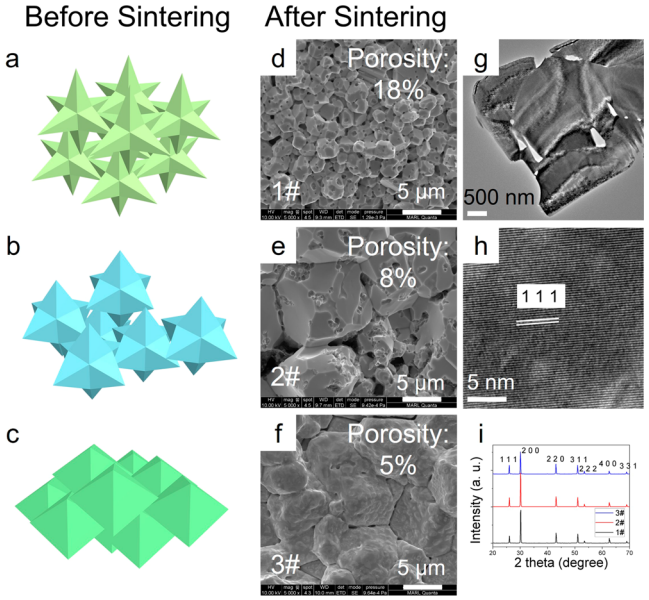

Figure 2. (a–c) Schematic illustration of the possible spatial packings of 1# (hexapods), 2# (less-protruding hexapods), and 3# (octahedra), respectively, (d–f) SEM images of the as-sintered 1# (from hexapods), 2# (from less-protruding hexapods,) and 3# (from octahedra) samples, scale bars, 5 μm, (g) low-magnification TEM (scale bar, 500 nm) and (h) HRTEM images (scale bar, 5 nm) of the FIB-fabricated thin section of the 1# sample, (i) XRD profiles of the as-sintered 1–3# samples.

elucidated that lower convexity of the building bock leads to higher packing density.

A closer investigation through scanning electron microscopy (SEM) (Figures 2d–f) revealed a gradual increase in the average grain size (1#, 2.1 μm; 2#, 4.0 μm; and 3#, 6.2 μm) of the high-temperature-sintered monolith as the convexity of starting nanocrystals declined (from 1# hexapod, 2# less-protruding hexapods, to 3# octahedra). This trend can be rationalized based on denser stacking of the regularly shaped octahedron and its higher propensity for grain growth. TEM observations provided further structural details. The crystal domains and pores could be discerned in the low-magnification TEM (Figure 2g). HRTEM unveiled that each of the grain was well crystallized (Figure 2h). Other characterizations such as XRD (Figure 2i) and EDS verified the phase and chemical composition. The matrix phase was rock-salt PbS, while a little bit of Br (0.3 atom %) was distributed throughout the matrix.

The successful fabrication of porous monoliths from differently shaped nanocrystals enable us to study their thermoelectric performance. All of the electrical and thermal transport properties were measured in the direction parallel to the SPS pressing. The samples were placed between a cold and a hot end while the temperature gradient and the electrical voltage across the two ends were simultaneously measured to calculate the Seebeck coefficients (S). The negative sign of S indicates n-type doping, which we infer to arise from Br ($4s^24p^5$) at the S ($3s^23p^4$) site. The absolute value of S increases steadily as temperature ascends (Figure 3a). This increase implies a behavior that is characteristic of a degenerate semiconductor.[26] The Seebeck coefficients of all the samples are nearly identical (Figure 3a).

The electrical conductivity (σ) was measured using the bar configuration and confirmed by a different method (Vander Pauw). The electron carrier density (n_H) was retrieved through Hall effect measurements and showed nearly constant values against temperature (Figure S6g), confirming the degenerate semiconductor behavior. The electron mobility ($\mu_H = \sigma/n_He$)

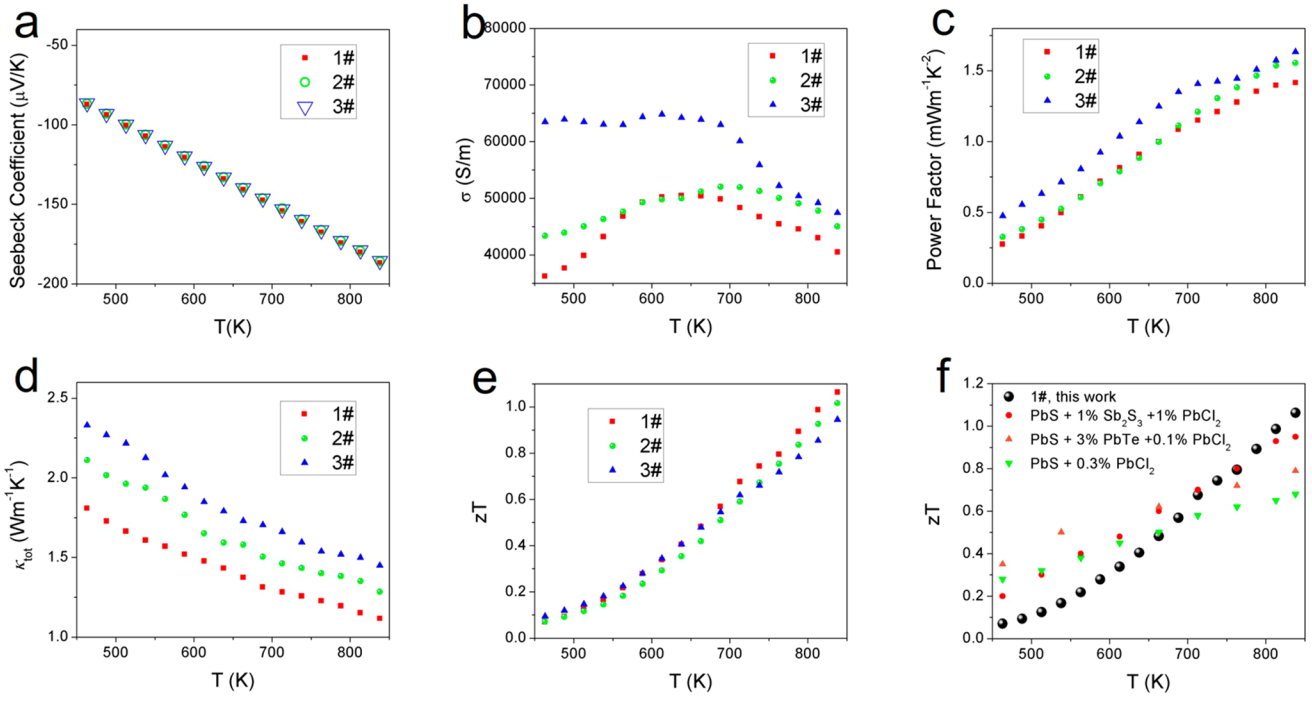

Figure 3. Temperature dependence of (a) Seebeck coefficient, (b) electrical conductivity, (c) power factor, (d) thermal conductivity, (e) zT of 1# (sintered from hexapods), 2# (sintered from less-protruding hexapods), and 3# (sintered from octahedra) samples. (f) The zT of our 1# sample in comparison with those of previously reported n-type PbS samples: PbS + 1% Sb_2S_3 + 1% $PbCl_2$,[26] PbS + 3% PbTe + 0.1% $PbCl_2$,[29] and PbS + 0.3% $PbCl_2$.[30]

DOI: 10.1021/acs.nanolett.8b01691
Nano Lett. 2018, 18, 4034–4039

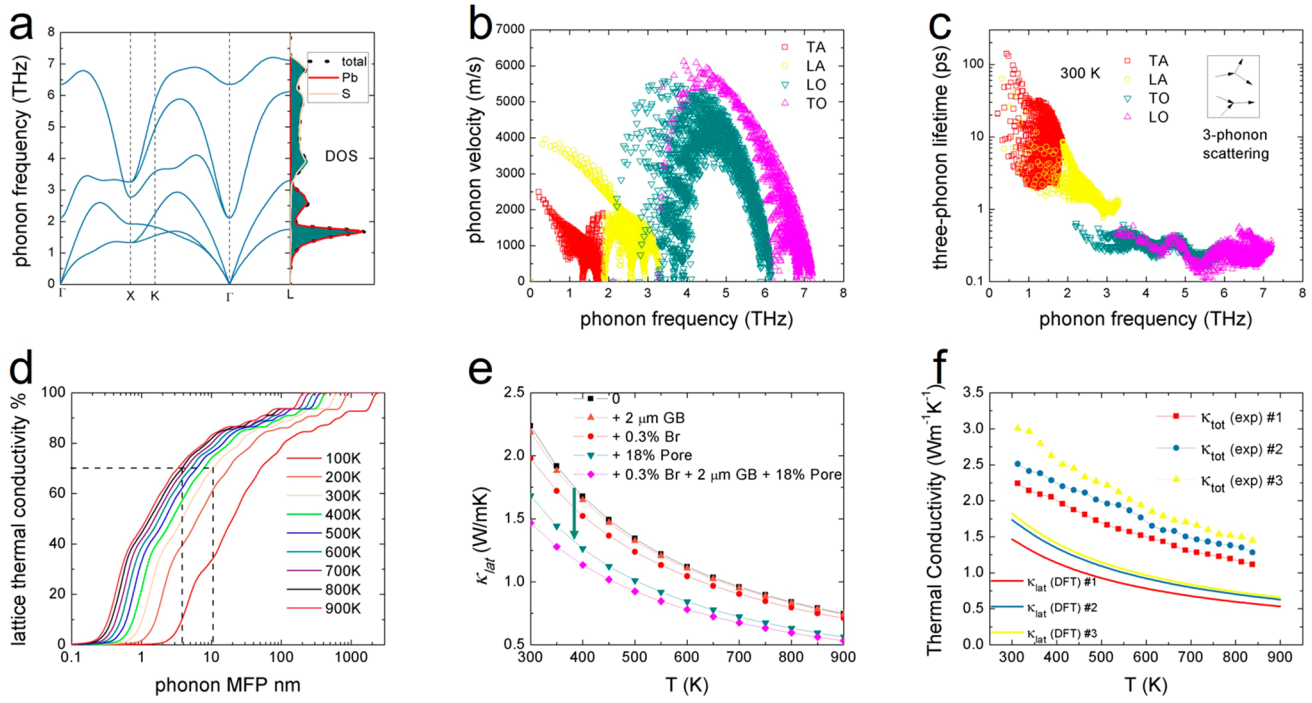

Figure 4. (a) Phonon dispersion, partial and total DOSs of pure PbS. (b) Phonon group velocity spectra of PbS. (c) Room-temperature phonon relaxation time spectra of PbS. (d) κ_{lat} cumulation with respect to phonon mean free path of PbS at different temperatures. (e) DFT calculated κ_{lat} of 1# by considering different phonon suppression mechanisms (grain boundary, 2 μm GB; alloying defect, 0.3% Br and 18% v/v pore (indicated by the arrow)). (f) DFT calculated κ_{lat} compared to the experimentally measured total thermal conductivities.

can be extracted from σ and n_H (Figure S6h). The temperature dependence of electrical conductivity (Figure 3b) is quite similar to those reported in the literature.[27,28] The non-monotonic trend is likely due to multiple scattering mechanisms of charge carriers. Because $\mu = e\tau/m^*$, in which τ is the carrier relaxation time and m^* is the carrier effective mass, if we assume the m^* to be constant with respect to temperature, the power exponent, δ, in the $\mu-T$ dependence, $\mu \propto T^{-\delta}$, can reflect the influence of different carrier scattering mechanism on τ. τ can be expressed by Matthiessen's rule: $1/\tau = 1/\tau_{e\text{-}ph} + 1/\tau_{e\text{-}II}$ in which the subscript, e-ph and e-II, denote the electron−phonon and electron−ionized impurity scattering, respectively.[27,28] Roughly, for the e-ph process, $\mu \propto T^{-1.5}$, while for the e-II process, $\mu \propto T^{1.5}$.[27,28] For our 1# sample (sintered from hexapods), at 450−600 K, μ is proportional to $T^{1.36}$ (Figure S6h), indicating the dominance of e-II scattering. At 650−850 K, μ is proportional to $T^{-0.86}$ (Figure S6h), suggesting that e-ph becomes the main scattering mechanism as phonons are excited at high temperature, but still mixes with the e-II. In the 2# and 3# samples, the scattering mechanisms are combinations of both e-ph and e-II at 450−600 K. At 650−850 K, e-ph again becomes the main mechanisms in 2# and 3# samples.

The power factor was calculated as $S^2\sigma$ and displayed in Figure 3c. Because the Seebeck coefficients of all the samples are nearly identical (Figure 3a), the differences in power factor originates from different σ. As the n_H of 1−3# samples are nearly identical (Figure S6g), the decreased σ and $S^2\sigma$ with respect to increased porosity (from 3# to 1#) can be ascribed to the impaired μ_H due to enhanced scattering of electrons by the pores.

The total thermal conductivity (κ_{tot}, Figure 3d) was calculated as $D_t \times \rho \times C_p$[26] in which D_t (thermal diffusivity) was measured using a laser flash method, ρ (mass density) was determined geometrically, and C_p (specific heat) was measured using differential scanning calorimetry (DSC). The κ_{tot} also decreases as the porosity increases (from 3# to 1#, Figure 3d), following the same trend of σ due to the scattering of phonons by pores.

Collectively, the thermoelectric figure of merit, zT is calculated as $S^2\sigma T/\kappa$ (Figure 3e). Although the 1# sample has the lowest relative density (82%) and largest portions of pores (18% v/v), its zT (1.06 at 838 K) is the best. We have also found a similar trend of the electrical and thermal transport properties in the other series of nanocrystals that have different convexity along the ⟨1 0 0⟩ directions (Figure S6).

We have conducted theoretical studies to reveal the origin of the excellent thermoelectric performance of our porous PbS materials. To study the influence of microstructure, especially the pores, on the lattice thermal conductivities (κ_{lat}), first-principles density functional theory (DFT)-based phonon Boltzmann transport equation (BTE) was employed. The κ_{lat} of nanoporous materials can be calculated by[31,32]

$$k_{lat} = \frac{1}{NV_{cell}}(1-P)\sum_{j}^{6}\sum_{\mathbf{q}}\frac{\hbar^2\omega^2(\mathbf{q},j)}{k_BT^2}\frac{e^{\hbar\omega(\mathbf{q},j)/k_BT}}{(e^{\hbar\omega(\mathbf{q},j)/k_BT}-1)^2} \upsilon_{ph,x}{}^2(\mathbf{q},j)\tau_{ph}(\mathbf{q},j), \quad (1)$$

$$\frac{1}{\tau_{ph}(\mathbf{q},j)} = \frac{1}{\tau_{anh}(\mathbf{q},j)} + \frac{1}{\tau_{iso}(\mathbf{q},j)} + \frac{1}{\tau_{def}(\mathbf{q},j)} + \frac{1}{\tau_{gb}(\mathbf{q},j)} + \frac{1}{\tau_{pore}(\mathbf{q},j)} \quad (2)$$

In eq 1, $\hbar$ is the Plank constant, k_B is the Boltzmann constant, T is temperature in Kelvin, $\omega(\mathbf{q}, j)$ is the perfect-crystal phonon angular frequency, $\mathbf{q}$ is the phonon wavevector,

DOI: 10.1021/acs.nanolett.8b01691
Nano Lett. 2018, 18, 4034−4039

Table 1. Comparison between the Present and Literature-Reported Properties of PbS

sample description	sintering condition	relative density	κ_{lat}[a] (W/mK)	μ_H[a] ($cm^2\ V^{-1}\ s^{-1}$)	$(\mu_H/\kappa_{lat})\cdot(m^*/m^0)^{3/2}$[a] ($10^{-3}\ m^3\ KV^{-1}\ s^{-1}\ W^{-1}$)	zT[a]
this work, 1# PbS	550 °C, 40 MPa, 5 min	82.2%	0.56	39.6	1.73	1.06
Zhao, PbS + 1% Sb_2S_3 + 1% $PbCl_2$[26]	550 °C, 60 MPa, 10 min	97.6%[b]	0.62	40[c]	1.57	0.95
Johnsen, PbS + 3% PbTe + 0.1% $PbCl_2$[29]	450 °C, 72 h	99%	0.73[d]	39[c]	1.39	0.8
Wang, PbS + 0.3% $PbCl_2$[30]	723 °C, 44 MPa, 30 min	99%	1.0	40	0.97	0.7

[a]All the values are measured at 838 K. [b]Calculated from $\rho = \kappa_{tot}/D_t/C_p$. [c]Calculated from $\mu_H = \sigma/n_H/e$, σ retrieved from power factor/S^2. [d]Calculated from $\kappa_{lat} = \kappa_{tot} - \kappa_e$.

j is the phonon branch, $v_{ph,x}$ is the phonon group velocity component in direction x, N is the number of $\mathbf{q}$ points sampled uniformly throughout the first Brillouin zone, and V_{cell} is the volume of a primitive unit cell. The summation is taken over all the phonon modes ($\boldsymbol{q}$, j). The effect of nano pores is studied beyond the effective medium approximation by taking into account the phonon-pore scattering. P is the porosity and the factor $(1 - P)$ takes into account the loss of material.[32] In eq 2, τ_{ph} is the total phonon relaxation time, which involves multiple phonon scattering processes including anharmonic phonon scattering (τ_{anh}^{-1}), phonon−isotope scattering (τ_{iso}^{-1}), phonon−defect scattering (τ_{def}^{-1}), phonon−grain boundary scattering (τ_{gb}^{-1}), and phonon−pore scattering (τ_{pore}^{-1}). Equations 1 and 2 reflect the fact that we are treating lattice thermal conductivity as arising from perfect-crystal phonons that undergo scattering by other phonons, isotopes, defects (in this case substitutional Br impurities), grain boundaries, and pores. Explicit expressions for the corresponding relaxation times are given in Supporting Information.

The calculated phonon dispersion relations and density of states for crystalline PbS are shown in Figure 4a, in agreement with previous literature.[33−35] Details of the calculation of the τ's of the different scattering processes can be found in the Supporting Information. The phonon spectra of the velocity and relaxation time are shown in Figures 4b,c, respectively. It is found that the acoustic phonons have longer relaxation times while the optical phonons have larger velocities. Overall, the acoustic and optical phonons contribute 60% and 40% to the κ_{lat} of pristine PbS, respectively (Figure S8d). These results illustrate that the general Debye model, which only considers acoustic phonons, is not able to correctly model heat transport in these materials. We have also found that 70% of the κ_{lat} at 300 K is contributed by phonons with mean free path shorter than 10 nm (Figure 4d). This value is decreased to 4 nm when the temperature increases to 800 K (Figure 4d). These results indicate that the nanoengineering of PbS-based materials has a stringent requirement on the grain size. The lattice thermal conductivity can be substantially suppressed by the grain boundaries only when the grain size is down far below 20 nm. In our samples, the grain sizes are of several micrometers and thus have very little influence on the κ_{lat} as seen in Figures 4e and S8a,b.

The calculated lattice thermal conductivities (κ_{lat}) of these samples are compared to the experimentally measured data in Figure 4f. It can be seen that lattice vibrations contribute over one-half to the total thermal conductivity. The remainder of the measured thermal conductivity can be attributed by an electronic contribution. The engineered structure of the material, including defects (0.3% Br impurities), grain boundaries, and pores (18% v/v) suppress the lattice thermal conductivity by 35−30% in the temperature range from 300 to 900 K for the 1# sample. The effect of nano pores contributes the most among various phonon suppression mechanisms to the reduction of κ_{lat}, as shown in Figures 4e and S8a,b. For the 2# and 3# samples, the decreased porosity as compared to 1# sample results in a smaller reduction of κ_{lat} by the pores (Figures S8a−c).

According to the theoretical analysis, the increased porosity that originates from increased convexity of the starting PbS nanocrystals can significantly reduce κ_{lat}. At the same time, the large grain size and the well-maintained crystallinity preserve a high carrier mobility (μH) and electron conductivity (σ), leading to an enhanced figure of merit, zT. This can be understood from the materials parameter,[36] $\beta = (\mu_H/\kappa_{lat})\cdot(m^*/m_0)^{3/2}$ (Table 1), which takes into account the carrier mobility and lattice thermal conductivity in the numerator and denominator, respectively. Because of the large grain size (2 μm) of our PbS sample (1#), the μ_H is high among those of state-of-the-art bulk-grain PbS materials (Table 1). Meanwhile, κ_{lat} of our porous PbS is lowest as compared to these denser PbS materials (Table 1). Collectively, the peak zT value (1.06 at 838 K) of the most porous sample (1#) is among the best of state-of-the-art PbS materials[26,29,30] (Figure 3f and Table 1), while the relative density (82%) is the lowest among these counterparts (Table 1). The high zT at 713−838 K (Figure 3f) qualifies our porous PbS material as a promising candidate in this temperature range. Thus, the improvement of performance and portability can be achieved simultaneously using our strategy involving shape-controlled nanocrystals.

In conclusion, we have developed a new strategy that utilizes solution-synthesized, convexity-controlled nanocrystals to fabricate porosity-tunable thermoelectric materials. The as-obtained porous monolith with large grain size exhibits high electrical conductivity, low thermal conductivity, and excellent zT (1.06 at 838 K), as well as possessing low relative mass density (82%) and high portability. The origin of high zT that can be attributed to enhanced scattering of phonons by the porous structures is studied by DFT calculations. We anticipate that by carefully controlling the domain structure and morphology of nanocrystals through solution synthesis, this strategy can be extended to fabricate other types of porous thermoelectric materials (e.g., PbSe, PbTe, and SnSe) and even porous materials with other functionalities, such as catalysis, photovoltaics, energy storage, and optoelectronics.

■ ASSOCIATED CONTENT

Supporting Information

The Supporting Information is available free of charge on the ACS Publications website at DOI: 10.1021/acs.nanolett.8b01691.

DOI: 10.1021/acs.nanolett.8b01691
Nano Lett. 2018, 18, 4034−4039

Experimental Section, more characterization details including XRD, TEM, and thermoelectric measurement, and theoretical modeling of lattice thermal conductivity (PDF)

AUTHOR INFORMATION

Corresponding Authors

*E-mail: xubiao@njust.edu.cn.
*E-mail: yuewu@iastate.edu.

ORCID

Tianli Feng: 0000-0002-7284-5657
Yue Wu: 0000-0002-9820-2000

Author Contributions

B.X. and Z.L. performed the synthesis of nanocrystal, TEM, XRD, SEM, and thermoelectric measurements. T.F. and S.T.P. performed the DFT calculations. B.X., S.T.P., and Y.W. supervised the work.

Funding

Startup Funding of Nanjing University of Science and Technology (AE89991/043). ACRI Center Initiative from Iowa State University. Herbert L. Stiles Professorship from Iowa State University. Department of Energy Grant DE-FG0209ER46554. McMinn Endowment from Vanderbilt University. National Energy Research Scientific Computing Center (NERSC) User Facility funded through Contract No. DE-AC02−05CH11231.

Notes

The authors declare no competing financial interest.

ACKNOWLEDGMENTS

B.X. acknowledges support from startup funding of Nanjing University of Science and Technology (AE89991/043). B.X., Z.L., and Y.W. thank the support from ACRI Center Initiative from Iowa State University and Herbert L. Stiles Professorship. Theoretical work by T.F. and S.T.P. was supported in part by Department of Energy Grant DE-FG0209ER46554 and by the McMinn Endowment. Computations at Vanderbilt University and ORNL were performed at the National Energy Research Scientific Computing Center (NERSC), a Department of Energy, Office of Science, User Facility funded through Contract No. DE-AC02-05CH11231. Computations also used the Extreme Science and Engineering Discovery Environment (XSEDE).

REFERENCES

(1) Yin, Y.; Rioux, R. M.; Erdonmez, C. K.; Hughes, S.; Somorjai, G. A.; Alivisatos, A. P. *Science* **2004**, *304*, 711.
(2) Tian, N.; Zhou, Z.-Y.; Sun, S.-G.; Ding, Y.; Wang, Z. L. *Science* **2007**, *316*, 732.
(3) Shen, L.; Yu, L.; Wu, H. B.; Yu, X.-Y.; Zhang, X.; Lou, X. W. *Nat. Commun.* **2015**, *6*, 6694.
(4) Sun, S.; Murray, C. B.; Weller, D.; Folks, L.; Moser, A. *Science* **2000**, *287*, 1989.
(5) Lee, J.-S.; Kovalenko, M. V.; Huang, J.; Chung, D. S.; Talapin, D. V. *Nat. Nanotechnol.* **2011**, *6*, 348.
(6) Kang, Y.; Ye, X.; Chen, J.; Qi, L.; Diaz, R. E.; Doan-Nguyen, V.; Xing, G.; Kagan, C. R.; Li, J.; Gorte, R. J.; Stach, E. A.; Murray, C. B. *J. Am. Chem. Soc.* **2013**, *135*, 1499.
(7) Zeng, H.; Li, J.; Liu, J. P.; Wang, Z. L.; Sun, S. *Nature* **2002**, *420*, 395.
(8) Urban, J. J.; Talapin, D. V.; Shevchenko, E. V.; Kagan, C. R.; Murray, C. B. *Nat. Mater.* **2007**, *6*, 115.
(9) Gong, J.; Newman, R. S.; Engel, M.; Zhao, M.; Bian, F.; Glotzer, S. C.; Tang, Z. *Nat. Commun.* **2017**, *8*, 14038.
(10) Henzie, J.; Grünwald, M.; Widmer-Cooper, A.; Geissler, P. L.; Yang, P. *Nat. Mater.* **2012**, *11*, 131.
(11) Lin, H.; Lee, S.; Sun, L.; Spellings, M.; Engel, M.; Glotzer, S. C.; Mirkin, C. A. *Science* **2017**, *355*, 931.
(12) Diroll, B. T.; Greybush, N. J.; Kagan, C. R.; Murray, C. B. *Chem. Mater.* **2015**, *27*, 2998.
(13) Wang, T.; Zhuang, J.; Lynch, J.; Chen, O.; Wang, Z.; Wang, X.; LaMontagne, D.; Wu, H.; Wang, Z.; Cao, Y. C. *Science* **2012**, *338*, 358.
(14) Tan, G.; Zhao, L.-D.; Kanatzidis, M. G. *Chem. Rev.* **2016**, *116*, 12123.
(15) Yang, L.; Chen, Z.-G.; Dargusch, M. S.; Zou, J. *Adv. Energy Mater.* **2018**, *8*, 1701797.
(16) Heremans, J. P.; Jovovic, V.; Toberer, E. S.; Saramat, A.; Kurosaki, K.; Charoenphakdee, A.; Yamanaka, S.; Snyder, G. J. *Science* **2008**, *321*, 554.
(17) Pei, Y.; Shi, X.; LaLonde, A.; Wang, H.; Chen, L.; Snyder, G. J. *Nature* **2011**, *473*, 66.
(18) Wu, D.; Pei, Y.; Wang, Z.; Wu, H.; Huang, L.; Zhao, L.-D.; He, J. *Adv. Funct. Mater.* **2014**, *24*, 7763.
(19) Poudel, B.; Hao, Q.; Ma, Y.; Lan, Y.; Minnich, A.; Yu, B.; Yan, X.; Wang, D.; Muto, A.; Vashaee, D.; Chen, X.; Liu, J.; Dresselhaus, M. S.; Chen, G.; Ren, Z. *Science* **2008**, *320*, 634.
(20) Kim, S. I.; Lee, K. H.; Mun, H. A.; Kim, H. S.; Hwang, S. W.; Roh, J. W.; Yang, D. J.; Shin, W. H.; Li, X. S.; Lee, Y. H.; Snyder, G. J.; Kim, S. W. *Science* **2015**, *348*, 109.
(21) Zhao, L.-D.; Lo, S.-H.; Zhang, Y.; Sun, H.; Tan, G.; Uher, C.; Wolverton, C.; Dravid, V. P.; Kanatzidis, M. G. *Nature* **2014**, *508*, 373.
(22) Son, J. S.; Choi, M. K.; Han, M.-K.; Park, K.; Kim, J.-Y.; Lim, S. J.; Oh, M.; Kuk, Y.; Park, C.; Kim, S.-J.; Hyeon, T. *Nano Lett.* **2012**, *12*, 640.
(23) Han, G.; Popuri, S. R.; Greer, H. F.; Bos, J.-W. G.; Zhou, W.; Knox, A. R.; Montecucco, A.; Siviter, J.; Man, E. A.; Macauley, M.; Paul, D. J.; Li, W.-g.; Paul, M. C.; Gao, M.; Sweet, T.; Freer, R.; Azough, F.; Baig, H.; Sellami, N.; Mallick, T. K.; Gregory, D. H. *Angew. Chem., Int. Ed.* **2016**, *55*, 6433.
(24) Huang, T.; Zhao, Q.; Xiao, J.; Qi, L. *ACS Nano* **2010**, *4*, 4707.
(25) Miszta, K.; de Graaf, J.; Bertoni, G.; Dorfs, D.; Brescia, R.; Marras, S.; Ceseracciu, L.; Cingolani, R.; van Roij, R.; Dijkstra, M.; Manna, L. *Nat. Mater.* **2011**, *10*, 872.
(26) Zhao, L.-D.; Lo, S.-H.; He, J.; Li, H.; Biswas, K.; Androulakis, J.; Wu, C.-I.; Hogan, T. P.; Chung, D.-Y.; Dravid, V. P.; Kanatzidis, M. G. *J. Am. Chem. Soc.* **2011**, *133*, 20476.
(27) Shuai, J.; Mao, J.; Song, S.; Zhu, Q.; Sun, J.; Wang, Y.; He, R.; Zhou, J.; Chen, G.; Singh, D. J.; Ren, Z. *Energy Environ. Sci.* **2017**, *10*, 799.
(28) Pan, L.; Mitra, S.; Zhao, L. D.; Shen, Y.; Wang, Y.; Felser, C.; Berardan, D. *Adv. Funct. Mater.* **2016**, *26*, 5149.
(29) Johnsen, S.; He, J.; Androulakis, J.; Dravid, V. P.; Todorov, I.; Chung, D. Y.; Kanatzidis, M. G. *J. Am. Chem. Soc.* **2011**, *133*, 3460.
(30) Wang, H.; Schechtel, E.; Pei, Y.; Snyder, G. J. *Adv. Energy Mater.* **2013**, *3*, 488.
(31) Feng, T.; Ruan, X. *J. Nanomater.* **2014**, *2014*, 206370.
(32) Dettori, R.; Melis, C.; Cartoixà, X.; Rurali, R.; Colombo, L. *Phys. Rev. B: Condens. Matter Mater. Phys.* **2015**, *91*, 054305.
(33) Zhang, Y.; Ke, X.; Chen, C.; Yang, J.; Kent, P. R. C. *Phys. Rev. B: Condens. Matter Mater. Phys.* **2009**, *80*, 024304.
(34) Wei, L.; Chen, J.-f.; He, Q.-y.; Teng, W. *J. Alloys Compd.* **2014**, *584*, 381.
(35) Skelton, J. M.; Parker, S. C.; Togo, A.; Tanaka, I.; Walsh, A. *Phys. Rev. B: Condens. Matter Mater. Phys.* **2014**, *89*, 205203.
(36) Hu, L.-P.; Zhu, T.-J.; Wang, Y.-G.; Xie, H.-H.; Xu, Z.-J.; Zhao, X.-B. *NPG Asia Mater.* **2014**, *6*, e88.

DOI: 10.1021/acs.nanolett.8b01691
Nano Lett. 2018, 18, 4034−4039

Supporting Information
for

Constructing Highly Porous Thermoelectric Monoliths with High Performance and Improved Portability from Solution-Synthesized Shape-Controlled Nanocrystals

Biao Xu,[a, b]* Tianli Feng,[c, d] Zhe Li,[b] Sokrates T. Pantelides[c, d] and Yue Wu.[b]*

[a] Prof. B. Xu
School of Chemical Engineering
Nanjing University of Science and Technology
Nanjing, Jiangsu 210094, China
E-mail: xubiao@njust.edu.cn

[b] Prof. B. Xu, Z. Li, Prof. Y. Wu
Department of Chemical and Biological Engineering
Iowa State University
Ames, Iowa 50011, USA
E-mail: yuewu@iastate.edu

[c] Dr. T. L. Feng, Prof. S. T. Pantelides
Department of Physics and Astronomy and Department of Electrical Engineering and Computer Science
Vanderbilt University
Nashville, Tennessee 37235, USA

[d] Dr. T. L. Feng, Prof. S. T. Pantelides
Materials Science and Technology Division
Oak Ridge National Laboratory
Oak Ridge, Tennessee 37831, USA

Biao Xu*: E-mail: xubiao@njust.edu.cn Tel: +86-13913857564

Yue Wu*: E-mail: yuewu@iastate.edu Tel: +1-(617) 871-9158

Table of Contents

1. **Experimental Procedures**

Reagents

Lead acetate trihydrate ($Pb(CH_3COO)_2 \cdot 3H_2O$, 99.99%), thioacetamide (CH_3CSNH_2, 99%), acetic acid (CH_3COOH, 98%) and cetyl trimethyl ammonium bromide (CTAB, 99%) were purchased from Sigma-Aldrich. Ultra-pure H_2O (18.2 MΩ·cm) was used throughout the synthesis. Ethanol (95%) and $N_2H_4 \cdot H_2O$ (80%) were purchased from VWR.

Syntheses

1# (hexapod), 2# (less-protruding hexapod) and 3# (octahedron):

45 mmol of $Pb(CH_3COO)_2 \cdot 3H_2O$ (17.0703 g), 45 mmol of thioacetamide (3.3756 g), 180 mmol of acetic acid (10.8090 g) and 11.25 mmol of CTAB (4.1004 g) were weighted and then dissolved into 1980 mL of H_2O. This solution is heated to 80°C under magnetic stirring and incubated for designated time. 1# (hexapod) sample was obtained after a reaction time of 5 h. The reaction time is 24 h for 2# (less-protruding hexapod) and 48 h for 3# (octahedron) samples. The as-obtained product weighted 6.4, 7.5 and 9.0 g for 1-3#.

The series of nanocrystals that the arms along the [1 0 0] axes are shortened into rectangular-shaped ones:

4# (hexapod), 5# (convex cube) and 6# (vertex-truncated cube):

The synthetic condition was as same as that of 1-3# nanocrystals except that the amount of thioacetamide was increased to 3.6X of stoichiometry (162 mmol, 12.1521 g). Then the 4# (hexapod), 5# (convex cube) and 6# (vertex-truncated cube) could be arrested at 5 h, 24 h and 48 h of the reaction, respectively. The as-obtained product weighted 10.2, 10.4 and 10.6 g for 4-6#.

Powder processing and spark plasma sintering

The solution-synthesized dispersion of nanocrystals was centrifuged and washed with warm (≈ 40°C) water for 2 times. Then it was re-dispersed in an ethanolic solution (800 mL) of 8% $N_2H_4 \cdot H_2O$ and stirred for 24 hrs. After this, the dispersion was centrifuged and washed by ethanol for 2 times. Then the slurry was vacuum-dried and ground into fine powder using an agate mortar. The powder was filled into a *Φ*-10 mm graphite die and loaded into a Spark Plasma Sintering system (Fuji-211*lx*, Fuji Electronic Industrial). The SPS parameters were set as follows: axial pressure: 40 MPa, sintering time: 5 min and temperature: 550°C.

Characterizations

X-ray diffraction (XRD) was conducted in a Bruker D8 Advance diffractometer, with Cu Kα radiation (*λ* = 1.5418 Å), at 40 kV and 44 mA. Scanning Electron Microscopy (SEM) images were acquired in a FEI Quanta 250, equipped with Energy Dispersion Spectra (EDS, Oxford Instrument). Transmission Electron Microscopy (TEM) was recorded in a FEI Tecnai F20 at 200 kV and a FEI Titan Themis *Cs*-corrected TEM at 300 kV. Thin-section samples of the as-sintered pellet for TEM were fabricated using a focused ion beam (FIB, Helios Dual Beam, FEI).

Transport measurement

The Seebeck coefficients (*S*) were measured in a Linseis LSR-3. The electrical conductivity (*σ*) was also measured in a Linseis LSR-3 using a four-probe configuration and re-confirmed by a

Van der-Pauw method (MMR Technology). The thermal conductivity (κ) was expressed as $\kappa = D_T * C_p * \rho$. Thermal diffusivity ($D_T$) was measured using laser flash method in a Linseis XFA 600. Specific heat (C_p) was measured in a Linseis differential scanning calorimeter (DSC) using sapphire as the standard. Mass density (ρ) was calculated from the sample mass and dimensions. Hall coefficients (R_H), carrier concentration (n_H) and resistivity (ρ) (Van der Pauw, 4-point probe) were measured simultaneously with a MMR Technology instrument using a 1 T magnet with pressure-assisted contacts. The electron mobility can be calculated as $\mu_H = \sigma/n_H e$.

The deviation of Seebeck coefficient is around 2%, electrical conductivity σ (5%) and thermal conductivity κ (5%). The combined uncertainty of zT ($S^2\sigma T/\kappa$) is around 15%.

2 Characterization Results

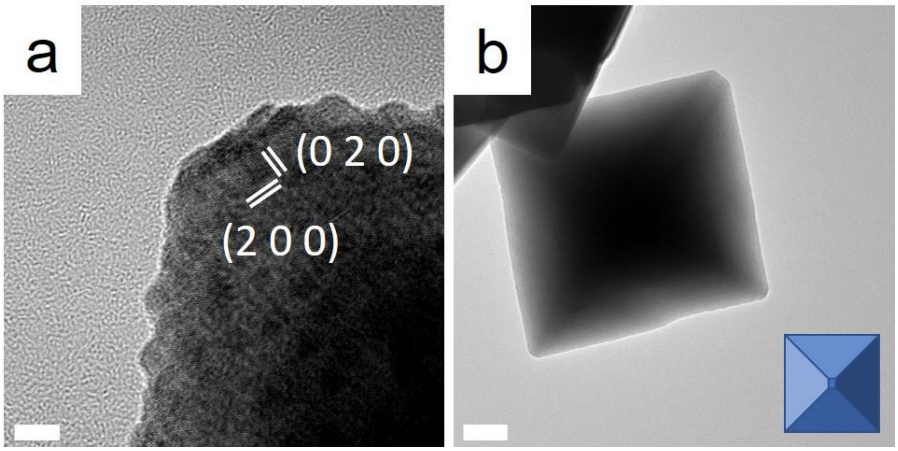

Figure S1. (a) HRTEM image of the octahedron (3# sample) along the [001] zone axis. Scale bar, 5 nm. (b) the low-magnification TEM of the octahedron (3# sample) along the [001] zone axis, scale bar is 50 nm. The inset shows the geometrical model.

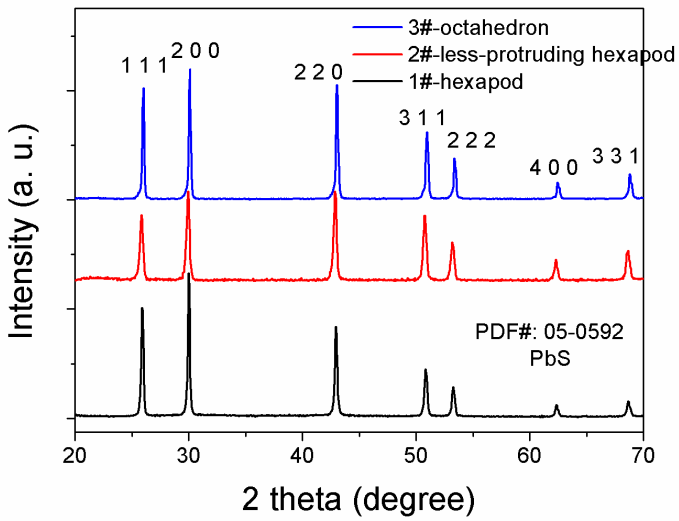

Figure S2. XRD profiles of the before-sintering samples: 1#, hexapod, 2# less-protruding hexapod and 3# octahedron nanocrystals.

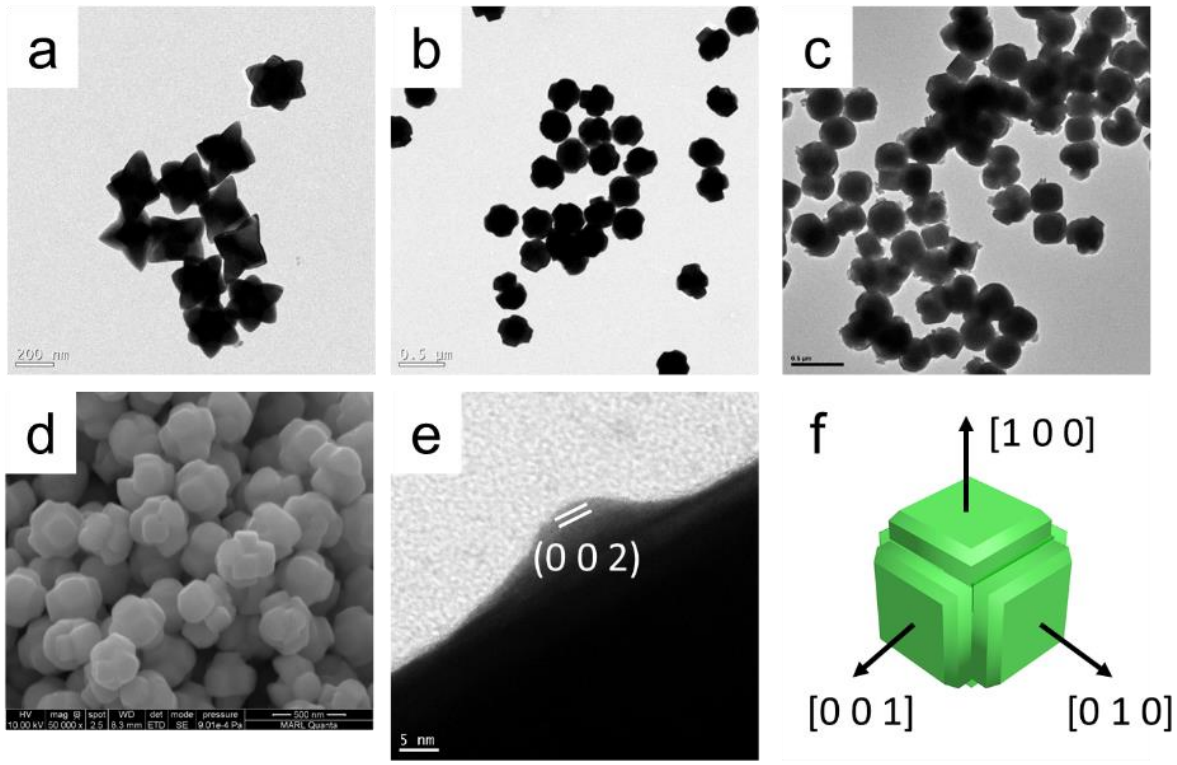

Figure S3. TEM images of the series of nanocrystals of which the arms along the [1 0 0] axes are shortened into rectangular-shaped ones: (a) 4# (hexapod), (b) 5# (convex cube) and (c) 6# (vertex-truncated cube). (d) SEM image, (e) HRTEM image and (f) schematic illustration of the facet orientation of the 5# (convex cube). The scale bars in (a)-(e) are 200 nm, 500 nm, 500 nm, 500 nm and 5 nm, respectively.

3 Models of the Spatial Packing of Hexapods

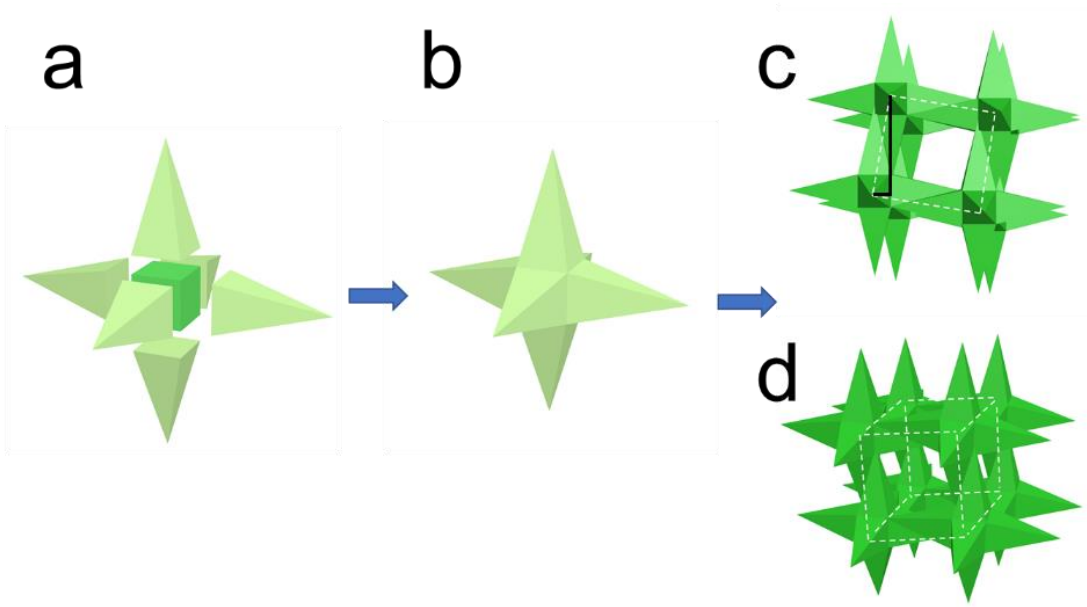

Figure S4. (a) 6 of square pyramids and one cube, (b) the as-assembled hexapod, (c) and (d) the illustrations of simple-cubic-symmetry assembly of the hexapods.

We proposed a possible model to calculate the packing density of PbS hexapods. The hexapod can be depicted as composed by six square pyramids attached onto a cube (Figure S4a, Castelli, A.; et al, Understanding and tailoring ligand interactions in the self-assembly of branched colloidal nanocrystals into planar superlattices. *Nature Communications* **2018,** *9* (1), 1141.). Based on the TEM observation in the main text (Figure 1a), the edge length of the cube is set as 200 nm, the length of the basal plane of the square pyramid is 200 nm and its height is 300 nm.
The hexapods are proposed to pack in the space in a simple cubic symmetry. Each arm is attached anti-parallelly to and share a lateral facet with another arm (Figure S4c and d). The tip end is attached to the vertex of the central, 200 nm-edge cube in the hexapod (Figure S4c and d). In this packing, the centers of the hexapods can be connected by the white dashed lines to form a cube showing the simple cubic symmetry (Figure S4d). The edge length of this dash-line cube can calculated as $\sqrt{(\frac{1}{2}\times 200)^2+(2\times\frac{1}{2}\times 200+300)^2}$ according to the black lines in Figure S4c.

Then the filling fraction of the packing can be calculated through dividing the volume of solid part of repeating unit by the volume of the dash-line cube. The solid part of repeating unit is composed by two parts: the 1st part is 1/8 of the central cube of the hexapod at 8 of the vertex of the dash-line cube, the 2nd part is 1/4 of the two square pyramids at 12 edges of the dash-line cube. Thus, the filling fraction can be calculated as:

$$\frac{8\times\frac{1}{8}\times 200^3+12\times\frac{1}{4}\times 2\times\frac{1}{3}\times 200^2\times 300}{[(\frac{1}{2}\times 200)^2+(2\times\frac{1}{2}\times 200+300)^2]^{3/2}}=24.1\%.$$

If we decrease the convexity, i. e., decrease the height of the square pyramid in the hexapod, we can obtain a higher filling fraction. For example, if the height of the square pyramid was decreased to 200 nm (Figure S5), the filling fraction can be calculated as:

$$\frac{8\times\frac{1}{8}\times200^3+12\times\frac{1}{4}\times2\times\frac{1}{3}\times200^2\times200}{[(\frac{1}{2}\times200)^2+(2\times\frac{1}{2}\times200+200)^2]^{3/2}}=34.2\%.$$

Figure S5. Illustration of the assembly of the less-protruding hexapods as compared to that in Figure S4.

If the height of the square pyramid was further reduced to 100 nm, the filling fraction can be calculated as:

$$\frac{8\times\frac{1}{8}\times200^3+12\times\frac{1}{4}\times2\times\frac{1}{3}\times200^2\times100}{[(\frac{1}{2}\times200)^2+(2\times\frac{1}{2}\times200+100)^2]^{3/2}}=50.6\%$$

4. Thermoelectric Data

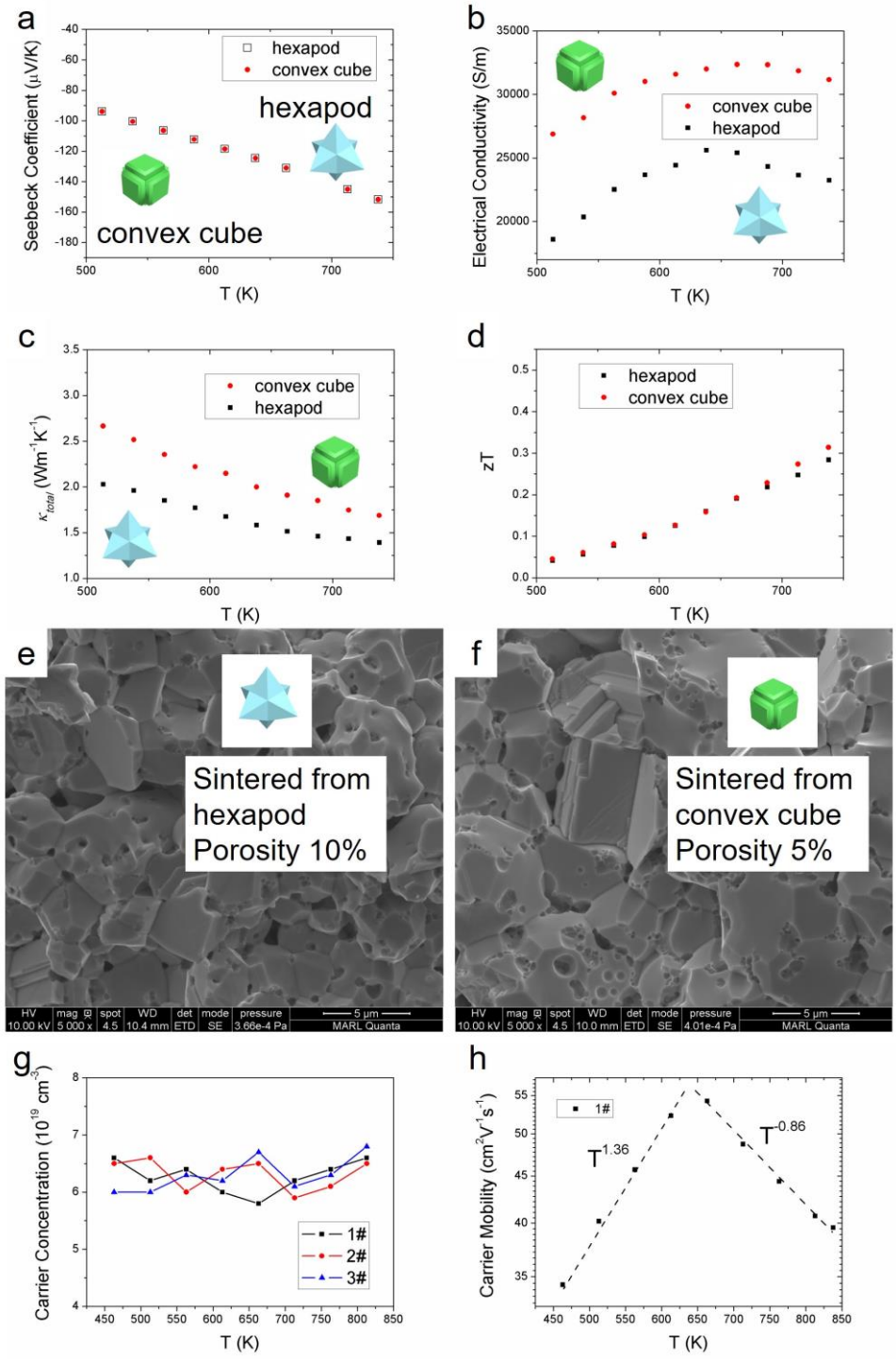

Figure S6. (a) Seebeck coefficient, (b) electrical conductivity, (c) thermal conductivity and (d) *zT* of the 4# (sintered from hexapods) and 5# (sintered from convex cubes) samples. SEM images of (e) 4# (sintered from hexapods) and (f) 5# (sintered from convex cubes) samples. (g) Hall-effect carrier concentration of the 1-3# samples. (h) carrier mobility (shown in a logarithmic scale) as a function of *T*.

According to EDS, the atomic percentage of Br is 0.3%. In 1 mol of '49.85 at% Pb + 49.85 at% S + 0.3 at% Br', there is 0.003 mol of Br. Assuming the complete ionization and doping of Br into the S site, it generates one electron. Thus, 0.003 mol of Br corresponds to $0.003*6.022*10^{23}$ of electrons. The mass of 1 mol of '49.85 at% Pb + 49.85 at% S + 0.3 at% Br can be calculated as 207.2*0.498 + 32.07*0.498 + 79.90*0.003 = 119.6 g. As the density of PbS is 7.5 $g \cdot cm^{-3}$, the volume is 119.6/7.5 = 15.95 cm^3. Therefore, the theoretical carrier concentration is $0.003*6.022*10^{23}/15.95\ cm^3 = 1.13*10^{20}\ cm^{-3}$. The doping efficiency of the 1# sample can be calculated as $6.50*10^{19}/1.13*10^{20}$ = 57.5%.

The main differences between zT of 5# sample and zT of 3# sample result from the different electrical conductivity. Since the Seebeck coefficients are also nearly identical, indicating the same carrier concentration, the differences result from different carrier mobility. The 3# (sintered from octahedron) and 5# (sintered from truncated cubes) samples are sintered from different subunits in which the grain boundary are oriented in different crystal directions ([1 1 1] for 3# (octahedron) and [1 0 0] for 5# (truncated cubes)). We propose that the different carrier mobility along different crystal directions lead to the differences in between 3# and 5# samples.

5. Modeling of Lattice Thermal Conductivity

To obtain the lattice thermal conductivity by Eq. (1) [1,2] of the main text, we have calculated the phonon dispersion relations and anharmonic phonon scattering rates using first-principles density functional theory (DFT). The calculations were carried out with the VASP program package [3,4] using the projector augmented wave method [4] (PAW) in the local density approximation for exchange-correlation effects. The atoms in the primitive unit cell of crystalline PbS were relaxed using a convergence threshold of 10^{-8} eV for the total energy, and 10^{-7} eV/Å for the forces on each atom. The plane-wave energy cutoff is 450 eV. The electronic **k**-space integration was performed with the tetrahedron method, involving a Γ-centered 16×16×16 **k**-mesh. The relaxed lattice constant is 5.8488 Å. The phonon dispersion is calculated via 4×4×4 pristine supercells (128 atoms) by the finite displacement method using the PHONOPY package [5] with a Γ-centered 4×4×4 **k**-mesh. Spin-orbital coupling is not included as it is not critical for lattice vibration properties [6].

The calculated phonon dispersion relations and density of states are shown in Fig. 4a of the main text. They are in good agreement with previous literature [7–9]. It is seen from the partial density of states that the Pb and S atoms have clearly distinct contributions to the lattice vibrations: Pb atoms dominate the acoustic vibrations while S atoms control the optical vibrations. Later on, it will be seen that the acoustic and optical phonons contribute 60% and 40% lattice thermal conductivities, respectively. The phonon group velocity $v_{ph}(\mathbf{q},j)$ was calculated by using $v_{ph} = d\omega/d\mathbf{q}$. The velocity spectrum is shown in Fig. 4b with a phonon **q** mesh of 36×36×36. It was found that a large portion of optical phonons has even larger group velocity than acoustic phonons.

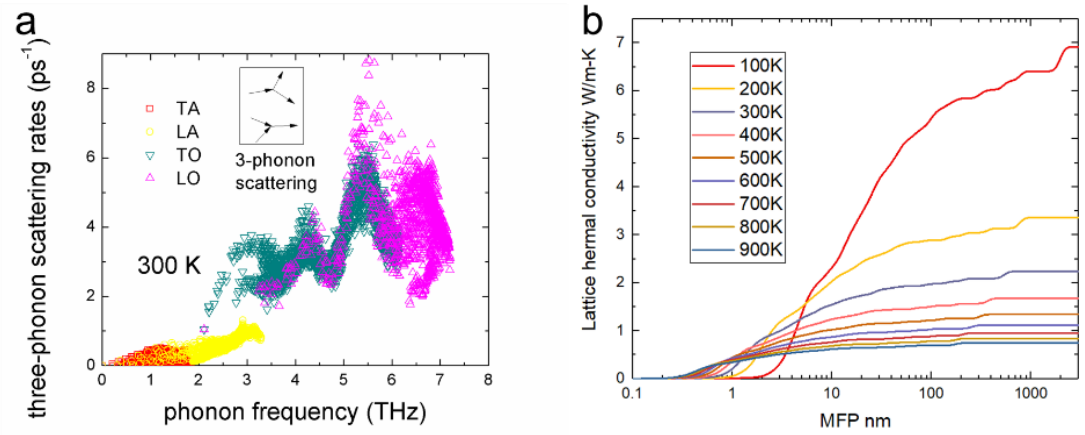

Figure S7. (a) The phonon spectral anharmonic scattering rates. (b) The accumulated thermal conductivity of pure PbS at different temperatures.

The anharmonic phonon scattering is calculated from first principles. The three-phonon scattering rate of a phonon mode $\lambda \equiv (\mathbf{q}, j)$ is the summation of the probabilities of all possible scattering events $\lambda \rightarrow \lambda_1 + \lambda_2$ (splitting) and $\lambda + \lambda_1 \rightarrow \lambda_2$ (recombination), where λ_1 and λ_2 are any other phonon modes $\lambda_1 \equiv (\mathbf{q_1}, j_1)$ and $\lambda_2 \equiv (\mathbf{q_2}, j_2)$. The scattering processes obey energy and quasi-momentum conservation rules: $\omega = \omega_1 + \omega_2$ and $\mathbf{q} = \mathbf{q_1} + \boldsymbol{q_2} + \boldsymbol{G}$ for splitting processes, $\omega + \omega_1 = \omega_2$ and $\mathbf{q} + \mathbf{q_1} = \boldsymbol{q_2} + \boldsymbol{G}$ for recombination processes. In the quasi-momentum conservation rule, a reciprocal lattice vector $\boldsymbol{G}$ can be involved, with $\boldsymbol{G} = \mathbf{0}$ and $\boldsymbol{G} \neq \mathbf{0}$ representing normal and Umklapp processes, respectively. The scattering rate is calculated by Fermi's golden rule (FGR) from DFT [10]:

$$\frac{1}{\tau_{anh}(\mathbf{q}, j)} = \sum_{\lambda_1, \lambda_2} \left(\frac{1}{2}(1 + f_{\lambda_1} + f_{\lambda_2})\vartheta_- + (f_{\lambda_1} - f_{\lambda_2})\vartheta_+ \right) \tag{1}$$

$$\vartheta_\pm = \frac{\pi\hbar}{4N_{\mathbf{q}}} \left| V_\pm^{(3)} \right|^2 \Delta_{\mathbf{q} \pm \mathbf{q}_1 - \mathbf{q}_2 + \mathbf{G}} \frac{\delta(\omega \pm \omega_1 - \omega_2)}{\omega \omega_1 \omega_2} \tag{2}$$

$$V_\pm^{(3)} = \sum_{b, l_1 b_1, l_2 b_2} \sum_{\alpha \alpha_1 \alpha_2} \phi_{0b, l_1 b_1, l_2 b_2}^{\alpha \alpha_1 \alpha_2} \frac{e_{\alpha b}^{\mathbf{q}, j} e_{\alpha_1 b_1}^{\pm \mathbf{q}_1, j_1} e_{\alpha_2 b_2}^{-\mathbf{q}_2, j_2}}{\sqrt{m_b m_{b_1} m_{b_2}}} \exp(\pm i \mathbf{q}_1 \cdot \mathbf{r}_{l_1} - i \mathbf{q}_2 \cdot \mathbf{r}_{l_2}) \tag{3}$$

where f_{λ_1} and f_{λ_2} are the phonon populations of the modes λ_1 and λ_2, which obey the Bose-Einstein distribution $f = \left(\exp(\frac{\hbar\omega}{k_B T}) - 1 \right)^{-1}$. ϑ_- and ϑ_+ are the scattering matrix elements which are determined by the third-order interatomic force constants ϕ. The indices b, l, and α represent basis atoms, primitive cells, and coordinate directions, respectively. m_b is the mass of the atom at the basis site b. $\mathbf{r}_l$ is the coordinate of the primitive cell l. $e_{\alpha b}^{\mathbf{q}, j}$ is the (α, b) component of the eigenvector of the phonon mode $(\mathbf{q}, j)$. The delta $\Delta_{\mathbf{q} \pm \mathbf{q_1} - \mathbf{q_2} + \boldsymbol{G}}$ describes the momentum selection rule and has the property that Δ_x= 1 (if x=0), or 0 (if x≠0). The delta function $\delta(\Delta\omega)$ is evaluated by using a Gaussian broadening function $\delta(\Delta\omega) = \frac{\sqrt{\pi}}{\epsilon} \exp(-\left|\frac{\Delta\omega}{\epsilon}\right|^2)$ where ϵ is an infinitesimal quantity. $\phi_{0b, l_1 b_1, l_2 b_2}^{\alpha \alpha_1 \alpha_2}$ are the third-order force constants, which are calculated from VASP DFT to the 6th nearest neighbor by using the Thirdorder package with ShengBTE. The $\mathbf{q}$ grid is taken as 36×36×36.

The three-phonon scattering rate spectra are shown in Fig. S7(a). The thermal conductivities at different temperatures and their accumulations are presented in Fig. S7(b). We find that the optical phonons have much larger scattering rates and thus much shorter relaxation times than acoustic phonons. Their relaxation times are 0.1-0.7 ps and 1-100 ps, respectively. The short relaxation times of optical phonons are partially compensated by their large group velocity, whereby their mean free path can reach up to 3 nm, which is still much shorter than most acoustic phonons. Despite the short MFP, the optical phonons still contribute 36% of the total lattice thermal conductivity of pure PbS at room temperature due to the large group velocity as shown in Fig. S8(b).

The isotope, defect, and grain boundary scattering rates are calculated by

$$\frac{1}{\tau_{iso}(\mathbf{q}, j)} = \frac{\pi}{2} g_{iso} \omega^2(\mathbf{q}, j) DOS(\omega) \tag{4}$$

$$\frac{1}{\tau_{def}(\mathbf{q}, j)} = \frac{\pi}{2} g_{def} \omega^2(\mathbf{q}, j) DOS(\omega) \tag{5}$$

$$\frac{1}{\tau_{gb}(\mathbf{q}, j)} = \frac{v_{ph}(\mathbf{q}, j)}{D_{grain}} \tag{6}$$

, respectively. [1,11–14] g_{iso} and g_{def} are the mass disorders induced by the natural Pb/S isotopes and the Br defects (0.3%) in the samples given by $g = \eta \left(\frac{\Delta M}{M}\right)^2$, where η is the concentration of isotopes (defects), and ΔM is the mass difference between isotopes (defects) and the pristine Pb/S atoms. $DOS(\omega)$ is the normalized density of states of the pristine PbS. [1,11–14] D_{grain} is the average grain diameter, which is 2, 4, 6 μm for the 1#, 2# and 3# samples, respectively.

The phonon-pore scattering is determined by [2]

$$\frac{1}{\tau_{pore}(\mathbf{q}, j)} = \frac{P}{2} \frac{1}{\tau_{bulk}(\mathbf{q}, j)} + \frac{3P v_{ph}(\mathbf{q}, j)}{2D_{pore}} \tag{7}$$

where D_{pore} is the average pore diameter, which is 0.5, 0.7, and 0.5 μm for the 1#, 2# and 3# samples, respectively. The porosity P is 18%, 8%, and 5% for the 1#, 2# and 3# samples, respectively.

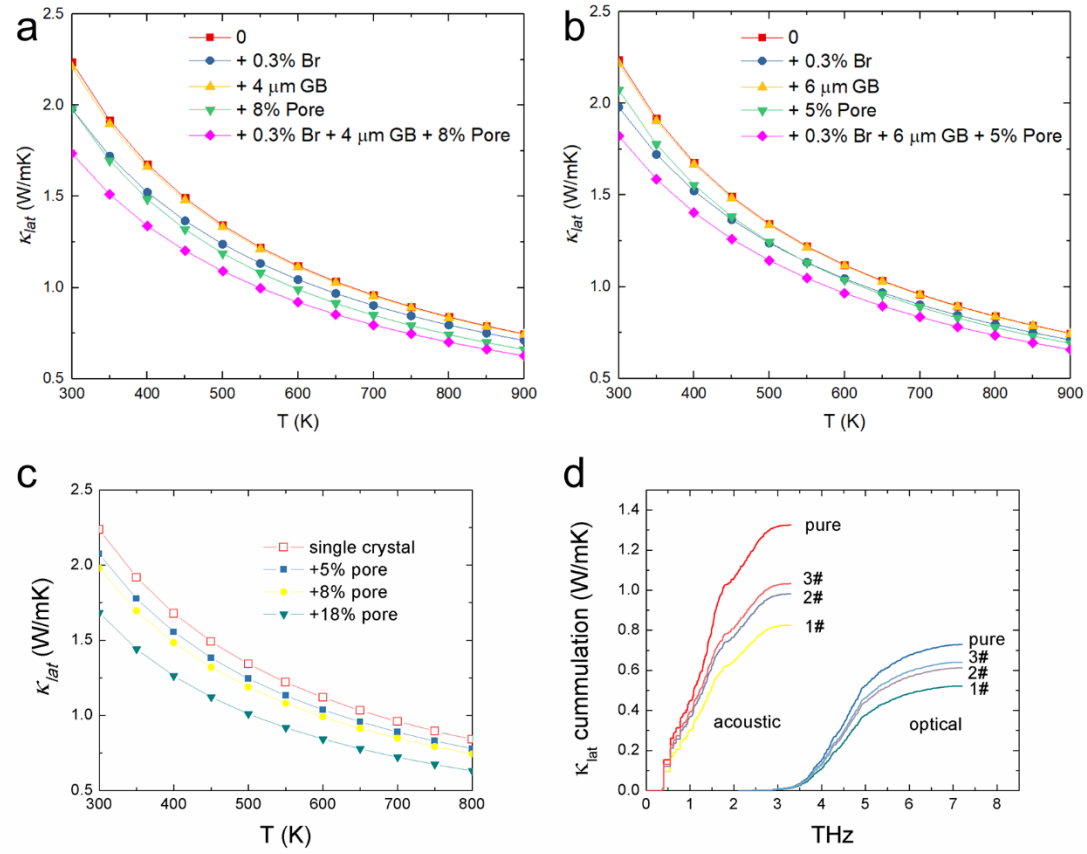

Figure S8. (a) (b) The contributions of different phonon scattering mechanisms to the lattice thermal conductivity reduction in #2 (sintered from less-protruding hexapods) and #3 samples (sintered from octahedra). (c) simulated influences of different porosity on κ_{lat}. (d) The lattice thermal conductivity accumulations as a function of phonon frequency for acoustic and optical phonons.

The calculated lattice thermal conductivities of these samples are compared to the experimentally measured data in Fig. 4f of the main text. It is seen that lattice vibrations contribute over 1/2 of the total thermal conductivity. The reduction of lattice thermal conductivity compared to pure PbS mainly results from the pores and impurities as shown in Fig. 4e, S8a and S8b. The relative contribution of optical phonons to the lattice thermal conductivity increases to 40% as shown in Fig. S8d.

References

[1] T. Feng and X. Ruan, J. Nanomater. **2014**, 206370 (2014).
[2] R. Dettori, C. Melis, X. Cartoixà, R. Rurali, and L. Colombo, Phys. Rev. B **91**, 1 (2015).
[3] G. Kresse and J. Hafner, Phys. Rev. B **47**, 558 (1993).
[4] G. Kresse and J. Furthmüller, Phys. Rev. B **54**, 11169 (1996).
[5] A. Togo, F. Oba, and I. Tanaka, Phys. Rev. B **78**, 134106 (2008).
[6] A. H. Romero, M. Cardona, R. K. Kremer, R. Lauck, G. Siegle, J. Serrano, and X. C. Gonze, Phys. Rev. B **78**,

224302 (2008).
[7] Y. Zhang, X. Ke, C. Chen, J. Yang, and P. Kent, Phys. Rev. B **80**, 024304 (2009).
[8] L. Wei, J. Chen, Q. He, and W. Teng, J. Alloys Compd. **584**, 381 (2014).
[9] J. M. Skelton, S. C. Parker, A. Togo, I. Tanaka, and A. Walsh, Phys. Rev. B - Condens. Matter Mater. Phys. **89**, 1 (2014).
[10] D. a. Broido, M. Malorny, G. Birner, N. Mingo, and D. a. Stewart, Appl. Phys. Lett. **91**, 231922 (2007).
[11] T. Feng, B. Qiu, and X. Ruan, Phys. Rev. B - Condens. Matter Mater. Phys. **92**, 1 (2015).
[12] S. Tamura, Phys. Rev. B **27**, 858 (1983).
[13] J. Garg, N. Bonini, B. Kozinsky, and N. Marzari, Phys. Rev. Lett. **106**, 045901 (2011).
[14] S. Huberman, V. Chiloyan, R. A. Duncan, L. Zeng, R. Jia, A. A. Maznev, E. A. Fitzgerald, K. A. Nelson, and G. Chen, Phys. Rev. Mater. **1**, 054601 (2017).